

1 **Using kinetic energy measurements from altimetry to detect shifts in the**  
2 **positions of fronts in the Southern Ocean**

3 Don P. Chambers<sup>1</sup>

4 <sup>1</sup> College of Marine Science, University of South Florida, St. Petersburg, FL

5 Correspondence to: D. Chambers ([donc@usf.edu](mailto:donc@usf.edu))

6

7 **Abstract.** A novel analysis is performed utilizing cross-track kinetic energy (CKE) computed  
8 from along-track sea surface height anomalies. The mid-point of enhanced kinetic energy  
9 averaged over three-year periods from 1993 to 2016 is determined across the Southern Ocean  
10 and examined to detect shifts in frontal positions, based on previous observations that kinetic  
11 energy is high around fronts in the Antarctic Circumpolar Current system due to jet instabilities.  
12 It is demonstrated that although the CKE does not represent the full eddy kinetic energy  
13 (computed from crossovers), the shape of the enhanced regions along groundtracks is the same,  
14 and CKE has a much finer spatial sampling of 6.9 km. Results indicate no significant shift in the  
15 front positions across the Southern Ocean, on average, although there are some localized, large  
16 movements. This is consistent with other studies utilizing sea surface temperature gradients, the  
17 latitude of mean transport, and probability of jet occurrence, but is inconsistent with studies  
18 utilizing the movement of contours of dynamic topography.

## 19 1. INTRODUCTION

20 There is as much we don't know about the circulation of the Southern Ocean as we do.  
21 Although the current system is routinely called the Antarctic Circumpolar Current (ACC), it  
22 consists of several fronts with distinct water properties to the north and south of the fronts  
23 (Nowlin and Clifford, 1982; Orsi et al., 1995; Belkin and Gordon, 1996). The most significant of  
24 these fronts, responsible for the majority of the ACC volume transport (e.g., Cunningham et al.,  
25 2003), are the Subantarctic Front (SAF) and the Polar Front (PF). However, even this is not a  
26 realistic picture of the circulation in the Southern Ocean, since at any specific time, there can be  
27 from three to ten narrow jets around the fronts that are highly variable in strength and location,  
28 masking the specific frontal boundary (Sokolov and Rintoul, 2007, 2009a, 2009b; Sallee et al.,  
29 2008; Thompson et al., 2010; Thompson and Richards, 2011; Langlais et al., 2011; Graham et  
30 al., 2012; Chapman, 2014; Gille, 2014; Kim and Orsi, 2014; Shao et al., 2015; Chapman, 2017a).  
31 Although positions of fronts have been estimated throughout the Southern Ocean, primarily  
32 using gradients of subsurface density measured from hydrographic sections (Orsi et al., 1995),  
33 contours of dynamic topography (Sokolov and Rintoul 2007, 2009a, 2009b; Langlais et al.,  
34 2011), or a combination Kim and Orsi (2014), in many places there are no strong currents that  
35 can be measured near the front position (Chapman, 2014; 2017a).

36 Because of the highly variable nature of jets and the lack of clear observational detection of  
37 fronts in some areas, the literature has become muddled over the difference between a front and a  
38 jet, primarily because the "front" is rarely observed at any specific time due to the high-  
39 variability of jets (Thompson et al., 2010; Thompson and Richards, 2011; Chapman 2014;  
40 2017a). However, even in the presence of highly variable jets, methods have been developed to  
41 determine mean fronts positions in a probabilistic sense. Thompson et al. (2010) demonstrated

42 one could define fronts in the Southern Ocean by computing probability density functions of  
43 potential vorticity in an eddy-resolving general ocean circulation model. Chapman (2014, 2017a)  
44 later showed this could also be done using localized gradients in dynamic topography (i.e., high  
45 geostrophic velocity) using satellite altimeter observations, but again, only as statistical  
46 probability. This is because these areas of enhanced gradients and velocity are more reflective of  
47 jets, which strengthen and die, appear and disappear, bifurcate and join back together. Because of  
48 this, they can only be detected on average 10-15% of the time. However, Chapman (2014,  
49 2017a) has demonstrated that, at least in a mean sense, fronts defined by mean dynamic  
50 topography contours (commonly known as the “contour method”) do lie within the probability  
51 distribution inferred from “gradient” methods.

52 An open question is how the fronts and jets that comprise the ACC will respond in a  
53 warming climate. Analysis of climate models (which cannot simulate jets in the Southern Ocean)  
54 suggests that as the atmosphere warms, the winds that drive the fronts and jets of the ACC will  
55 migrate south (e.g., Fyfe and Saenko, 2006; Swart and Fyfe, 2012). It should be noted, however,  
56 that the mean position of the southern hemisphere westerlies in the models lies significantly  
57 equatorward of the true position (e.g., Figure 2 in Fyfe and Saenko, 2006). Thus, it is not entirely  
58 clear whether the model is predicting a true shift in the wind position, or whether the model has  
59 not yet reached equilibrium with winds in the proper location.

60 Still, based on these model results, researchers have been testing the hypothesis that as winds  
61 in the Southern Ocean shift south, the frontal positions and jets will also migrate south. So far,  
62 the results are mixed. Using the contour method and tracking how the dynamic topography  
63 contours associated with a front position shift in time, Sokolov and Rintoul (2009b) found that  
64 the SAF and PF had both moved south by approximately 60 km over 15 years between 1993 and

65 2008. Kim and Orsi (2014) recently updated this analysis and found that while the average  
66 frontal position across the Southern Ocean indicates a strong southward shift, this is due  
67 primarily to substantial shifts only in the Indian Ocean sector. They found no significant shifts  
68 throughout the Pacific or Atlantic Ocean sectors using the contour method.

69 The primary assumption of these analyses is that if a contour of dynamic topography shifts  
70 south, it is uniquely caused by a front moving south. This is not necessarily true. Gille (2014)  
71 recently demonstrated that all contours in the Southern Ocean have shifted south on average, and  
72 that this follows from the observed rise in sea level – as the sea surface height rises, the contours  
73 will appear to shift south. While this breaks down at the far south and north of the ACC where  
74 dynamic topography gradients are small, these areas are far away from the PF and SAF and so  
75 have not been considered in previous analyses. Gille (2014) used a different measure to  
76 determine the position of the ACC fronts, based on the latitude of the mean surface transport of  
77 the ACC measured by altimetry, which is in essence a mean location of all the jets in the  
78 Southern Ocean. She found no significant shift on average, but considerable interannual  
79 variability, especially regionally.

80 Another factor other than sea level rise can cause the dynamic topography contour to shift  
81 south -- if the magnitude and width of the jet has changed. This is demonstrated in **Figure 1**,  
82 where we show the mean dynamic topography from two jet scenarios: 1) where the peak of two  
83 Gaussian shaped jets have shifted south, and 2) where the peak has not shifted, but the magnitude  
84 has decreased, the width has broadened, and the shape has become slightly skewed. Although the  
85 resulting topography profiles are not identical, they are similar, and both suggest a southward  
86 movement of dynamic topography contours.



87        Researchers using other methods also find little or no southern migration of the fronts or jets  
88 in the Southern Ocean as a whole. Graham et al. (2012) used a high-resolution model to show  
89 that the Polar Front and Subantarctic Front are constrained by bathymetry, even in increasing and  
90 shifting winds. Shao et al. (2015) utilized the skewness of sea level anomalies to identify front  
91 positions, and found no southward motion, but did find changes in the east Pacific correlated  
92 with the Southern Annual Mode. Chapman (2017a), using positions of fronts determined from  
93 the probability of jet locations, also found no significant southward movement, but high  
94 interannual variability. Finally, Freeman and Lovenduski (2016a) used weekly estimates of the  
95 Polar Front position determined from satellite sea surface temperature (SST) gradients to show  
96 no significant southward shift between 2002 and 2014 on average, except in the Indian Ocean.  
97 They also found a statistically significant northward shift of the PF in part of the south Pacific.

98        Thus, recent studies all agree that the Subantarctic Front and Polar Front have not shifted  
99 south, even though there is evidence the winds have shifted south in the austral summer months  
100 (Swart and Fyfe, 2012). It should be noted that when averaged over the full calendar year,  
101 however, there has been no significant shift in the wind position (Swart and Fyfe, 2012).

102        In this paper, we develop a new method to study linear shifts in the position of the fronts in  
103 the Southern Ocean, based on tracking the location of envelopes of kinetic energy measured by  
104 satellite altimetry. It is known from modeling studies that the front positions are associated with  
105 increased kinetic energy, due to instabilities in the jets and interactions with bathymetry  
106 (Thompson et al., 2010; Thompson and Richards, 2011). After demonstrating that kinetic energy  
107 computed from along-track satellite altimetry forms relatively wide envelopes of enhanced  
108 energy that occur within the probability range of jets and fronts (e.g., Chapman, 2017a), we track  
109 the positions of these envelopes from 1993 until 2016 to quantify if the envelopes have shifted

110 south by a statistically significant amount. Since kinetic energy is highest around fronts in the  
111 Southern Ocean (e.g., Thompson et al., 2010; Thompson and Richards, 2011; Chapman, 2017),  
112 it follows that if the fronts have shifted south, then the envelope of high kinetic energy should  
113 also move by a comparable amount. We do not purport that our method derives the actual  
114 position of either a front or a jet due to the relatively wide swath of enhanced kinetic energy on  
115 either side of fronts related to variability of jets. Instead, we only purport that it can indicate  
116 shifts in the frontal position, because if a front has shifted south by 100 km (for instance), then  
117 the band of enhanced kinetic energy should also shift south by a comparable amount. It is  
118 difficult to reconcile a frontal shift without a displacement of kinetic energy.

119 Since the kinetic energy calculation is based on estimating gradients of sea level anomalies,  
120 this approach is similar to other gradient methods for detecting fronts or jets (e.g., Chapman,  
121 2014; 2017a; Gille, 2014; Freeman and Lovenduski, 2016a). It differs from these approaches,  
122 however, in that instead of determining individual gradients and tracking these over time, it looks  
123 for regions of high gradients (i.e., high energy) surround by regions of low gradient (i.e., low  
124 energy). This allows us to detect envelopes for every time-period considered, instead of only a  
125 fraction of the time, allowing for better tracking of the change over time.

126 Section 2 will describe the data and methods used, while section 3 will present results,  
127 including evaluation of the method for detecting mean positions of fronts and for tracking their  
128 change over time. Section 4 will discuss the results in the context of previous studies and  
129 evaluate the usefulness of the method.

## 130 **2. DATA AND METHODS**

131 We utilize geostrophic surface current anomalies computed from the 24-year record of 1-Hz  
132 sea surface height (SSH) data along the TOPEX/Poseidon (T/P) groundtrack in the Southern

133 Ocean (**Figure 2**). The altimetry data used are from four separate altimeter missions:  
134 TOPEX/Poseidon (January 1993 – January 2002), Jason-1 (February 2002 – July 2008), Jason-2  
135 (August 2008 – August 2016), and Jason-3 (August 2016 – December 2016). Because the  
136 official TOPEX/Poseidon (T/P) geophysical data records (GDRs) have not been updated since  
137 the late 1990s, we utilize the corrected data products from the Integrated Multi-Mission Ocean  
138 Altimeter Data for Climate Research provided by Beckley et al. (2010) at the NASA PO.DAAC  
139 site ([https://podaac.jpl.nasa.gov/Integrated\\_Multi-Mission\\_Ocean\\_AltimeterData](https://podaac.jpl.nasa.gov/Integrated_Multi-Mission_Ocean_AltimeterData)). Jason-1 data  
140 are from the GDR-C version and were downloaded from the NASA PO.DAAC site in June 2010.  
141 Jason-2 are from the GDR-D version and were downloaded from NOAA NODC  
142 (<ftp://ftp.nodc.noaa.gov/pub/data.nodc/jason2>) between August 2012 and June 2016. Jason-3 are  
143 also from the GDR-D version and were downloaded from NOAA NODC  
144 (<ftp://ftp.nodc.noaa.gov/pub/data.nodc/jason3>) on August 7 and 8, 2017.

145 We utilize the 1-Hz along-track SSH data from the four altimeters and compute sea level  
146 anomalies by interpolating the DTU10 mean sea surface model (Andersen and Knudsen, 2009;  
147 [http://www.space.dtu.dk/english/Research/Scientific\\_data\\_and\\_models/downloaddata](http://www.space.dtu.dk/english/Research/Scientific_data_and_models/downloaddata)) to the  
148 SSH location using bilinear interpolation. The DTU10 mean sea surface model is based on SSH  
149 from multiple altimeters averaged over 17 years in a rigorous and consistent manner (Andersen  
150 and Knudsen, 2009). T/P, Jason-1, and Jason-2 data were all included. All recommended  
151 geophysical and surface corrections (e.g., water vapor, ionosphere, sea state bias, ocean tides,  
152 inverted barometer, etc) have been applied, to correct for biases introduced by atmospheric  
153 signal refraction and sea state effects (e.g., Chelton et al., 2001).

154 We utilize this record rather than the gridded products based on mapping SSH from multiple  
155 altimeters (e.g., Ducet et al., 2000; Pujol et al., 2016), because the along-track data have a finer

156 resolution in space (6.9 km along the groundtrack) and we recently demonstrated that the  
 157 mapped altimetry data underestimated eddy kinetic energy (EKE) throughout the Southern  
 158 Ocean compared to using along-track data by as much as 60-70% (Hogg et al., 2015). While the  
 159 along-track sea level anomalies are filtered to reduce noise and thus may attenuate some signal,  
 160 the filtering used (described later in this section), is less than that used for the mapped data,  
 161 which uses observations from as long as 20 days and 200 km away to influence the mapped  
 162 value. By filtering only alongtrack data, the time differences are small (a few minutes at most),  
 163 and the spatial influence is less than 100 km. Tests with unfiltered data accounting for estimated  
 164 random noise in the sea level anomaly data suggests attenuation of kinetic energy is minimal  
 165 with this approach and, more importantly, that the shape of the kinetic energy envelope does not  
 166 significantly change.

167 One can only compute EKE from alongtrack data at crossover points, where the ascending  
 168 and descending groundtracks cross (Figure 2). Knowing the groundtrack angle with the north  
 169 meridian ( $\theta$ ) one can compute the zonal ( $d\eta/dy$ ) and meridional gradients ( $d\eta/dx$ ) of SSHA  
 170 directly from the gradients of SSHA for the ascending pass ( $d\eta/dr_{asc}$ ) and descending pass  
 171 ( $d\eta/dr_{des}$ ) using simple geometry (Parke et al., 1987)

$$172 \quad \frac{d\eta}{dy} = \frac{\left[ \frac{d\eta}{dr_{asc}} - \frac{d\eta}{dr_{des}} \right]}{2 \sin \theta}, \quad \frac{d\eta}{dx} = \frac{\left[ \frac{d\eta}{dr_{asc}} + \frac{d\eta}{dr_{des}} \right]}{2 \cos \theta}, \quad (1)$$

173 noting that this formulation assumes the gradients represent the derivative of the northern SSHA  
 174 relative to the southern SSHA (for both the ascending and descending passes). Once this is  
 175 computed, the velocities can be computed directly from the zonal and meridional gradients:

176 
$$u = -\frac{g}{f} \frac{d\eta}{dy}, v = \frac{g}{f} \frac{d\eta}{dx}, \quad (2)$$

177 where  $g$  is the acceleration due to gravity, and  $f$  is the Coriolis parameter

178 This formulation assumes that the velocity field has not changed significantly between the  
 179 times the two passes fly over the crossover point. At high latitudes, the majority of crossovers (>  
 180 78%) have a time separation of less than 3 days. At 40°S, the average propagation speed of an  
 181 eddy is about 3 cm s<sup>-1</sup> [Chelton et al., 2007], meaning the eddy would have only been displaced  
 182 by 8 km at most over this period. At higher latitudes, this is even less. Considering the diameter  
 183 of eddies at these latitudes are of order 100 km [Chelton et al., 2007], the movement is not large  
 184 enough to cause a significant change in velocity at the point. The primary problem with  
 185 velocities computed from crossovers is the smaller number compared to using gridded data, or  
 186 the time-varying, anomalous geostrophic current normal to the groundtrack ( $u_T$ ). This can be  
 187 computed directly from the derivative of the SSH anomaly ( $\eta$ ) along the ground-track distance  
 188 ( $dr$ ) from

189 
$$u_T = -\frac{g}{f} \frac{d\eta}{dr} \quad (3)$$

190 This cross-track current is a projection of both the zonal ( $u$ ) and meridional ( $v$ ) components of  
 191 the full anomalous velocity field. However, neither  $u$  nor  $v$  can be determined unambiguously  
 192 from  $u_T$ . Here, we merely examine the variability of  $u_T$  without making any assumptions  
 193 concerning how it may be related to the full velocity, or  $u$  and  $v$ .

194 Because derivatives of SSHA (Equations 1 and 3) have to be computed numerically (here,  
 195 center-differences are used) and  $\eta$  contains significant noise at the 1 Hz sampling-rate of the  
 196 altimeters, we optimally interpolate  $\eta$  along-track using a model of the covariance of the signal

197 and error. We used the method of Wunsch (2006, Chapter 3) and a covariance function modeled  
198 as a Gaussian with a roll-off of 98 km and random noise of 2 cm, which was determined from the  
199 autocovariance of all TOPEX/Poseidon, Jason-1, and Jason-2 SSHA data from 1993-2015  
200 between 40°S and 65°S.

201 Once  $u_T(t)$  was computed at each 1-sec bin along the groundtracks in Figure 2 for each 10-  
202 day repeat cycle, the cross-track kinetic energy (CKE) was computed as  $CKE(x,t) = 0.5 u_T(x,t)^2$ ,  
203 where  $x$  here is used to denote a generic 1-sec bin along the ground track. We also computed the  
204 full EKE at the more limited crossover points as  $EKE(x,t) = 0.5(u(x,t)^2 + v(x,t)^2)$ .

205 The CKE values were averaged over the entire 24-year record and examined for each  
206 groundtrack segment (both ascending and descending) to judge where CKE was exceptionally  
207 high (Figure 3). We also computed CKE using the raw values of  $\eta$  with no optimal interpolation  
208 and compared to that computed with optimal interpolation. The locations of high CKE were the  
209 same, although values were significantly higher with the unsmoothed data. The quiescent regions  
210 of the ocean also showed considerably more noise, making it more difficult to determine  
211 boundaries of elevated CKE. For this reason, the values determined from the optimally  
212 interpolated data were used.

213 Several criteria were utilized to quantify where the high CKE values were considered to be  
214 associated with fronts. First, we constrained the southern boundary to be 5° south of the Orsi et  
215 al. (1995) values of the PF and the northern boundary to be 5° north of the SAF. Secondly, we  
216 used a lower-limit for CKE of  $200 \text{ cm}^2 \text{ s}^{-2}$  for detection and tested that the width of the envelope  
217 of high CKE above the lower-limit was at least 100 km. The requirement that the envelope be  
218 greater than 100 km was done to reduce the impact of eddies in an otherwise quiescent region,  
219 since the diameter of eddies in the Southern Ocean is about 100 km. The CKE lower-limit was

220 determined via iteration with different limits. For each case, the average center of the CKE  
221 envelope averaged over 24-years (based on the mean of the first and last points to exceed the  
222 lower-limit) was computed and compared visually to the Orsi et al. (1995) front positions. 200  
223  $\text{cm}^2 \text{ s}^{-2}$  was selected because there were a significant amount of CKE envelope centers clustered  
224 around the Orsi et al. (1995) fronts and the envelopes were found for every 10-day repeat cycle.  
225 Using a higher limit resulted in fewer detections, especially when smaller time-averages were  
226 used. Using a lower limit, we could find more potential front positions based on CKE, but many  
227 were far from the front positions estimated by Orsi et al (1995) and other authors (e.g., Kim and  
228 Orsi, 2014; Freeman and Lovenduski, 2016a; Chapman, 2017).

229 An example of a detected high CKE envelope is shown in Figure 3, based on the average of  
230 CKE between 1993 and 2015 computed from T/P-Jason satellite pass 207 in the south Indian  
231 Ocean. This pass starts at  $64.3^\circ\text{S}$  near the prime meridian and extends to  $41.2^\circ\text{S}$  and  $41^\circ\text{E}$   
232 longitude. There is clearly a wide envelope of enhanced CKE greater than  $200 \text{ cm}^2 \text{ s}^{-2}$  between  
233  $55^\circ\text{S}$  and  $47^\circ\text{S}$ .

234 The mean CKE profile pictured in Figure 3 has multiple local maxima, most likely associated  
235 with variability of the narrow jets that surround the front. They may also represent two separate  
236 fronts (and frontal-related jets) that are close in space. Some frontal climatologies find the SAF  
237 and PF are separated by fewer than 100 km in the South Indian Ocean (between  $30^\circ\text{E}$  and  $40^\circ\text{E}$ ),  
238 the South Pacific (between  $220^\circ\text{E}$  and  $230^\circ\text{E}$ ), and the South Atlantic ( $310^\circ\text{E}$  and  $330^\circ\text{E}$ ) (Figure  
239 2). CKE computed in these areas may encompass energy around both fronts. However, if the  
240 fronts have both shifted south (as reported in some studies), then CKE should also shift south  
241 and so tracking CKE should observe the shifts in frontal location.

242 Figure 4 shows the behavior of CKE along this pass for different 3-year periods. Note that

243 the number of clearly defined maxima ranges from a low of 4 for the 2014-2016 average to 9 in  
244 1993-1995. Note that even with a fixed and stationary front, there may be highly variable  
245 locations of peaks in CKE around the front, due to the meandering and disappearance/formation  
246 of jets (e.g., Chapman, 2017a). Thus, tracking the specific jet locations is not an optimal method  
247 of tracking frontal shifts. While other studies have estimated positions of these maxima in SSHA  
248 gradients on daily intervals (e.g., Chapman, 2017a), one does not obtain a consistent number of  
249 maxima each time, making the determination of shifts difficult. Moreover, note that although  
250 there are two general peaks in CKE in the long-term mean profile, the minimum between them is  
251 still higher than  $200 \text{ cm}^2 \text{ s}^{-2}$ . A minimum is also not well defined in several of the shorter  
252 averaging periods (for example, 2008-2010).

253 Thus, instead of attempting to track all the maxima of CKE individually – analogous to  
254 tracking steepest gradients, as in Thompson et al. (2010), Graham et al. (2012), or Chapman  
255 (2017a) – we track an estimate of the center of the envelope of enhanced CKE, as it exists in all  
256 averaging periods. The assumption we make in doing this is that the localized maxima are  
257 associated with variable jets, but the position of the envelope of high CKE is related to the  
258 general position of the front, and that if the front has systematically shifted then the CKE  
259 envelope will have shifted as well. Other studies have tracked the mean latitude of the integrated  
260 transport computed between dynamic height contours that are picked to represent the southern  
261 boundary and the northern boundary that encompass all the fronts in the ACC (Gille, 2014). One  
262 issue with this approach is how to uniquely determine the northern and southern boundary  
263 contours without potentially biasing the result (e.g., using a priori fixed boundaries and ignoring  
264 that they might have shifted). The method we propose will determine the boundaries of the  
265 integration uniquely for each pass based solely on the level of CKE relative to the peak of the



266 enhanced CKE envelope. Moreover, it allows for two or more distinct CKE envelopes along  
 267 each pass (i.e., related to different fronts), whereas the Gille (2014) method can only compute  
 268 one mean latitude for all fronts in the between the prescribed southern and northern boundaries.  
 269 Thus, our method is more flexible in determining boundaries around any particular front,  
 270 provided the orientation of the groundtrack is such that the majority of jets are perpendicular to  
 271 it.

272 There are many different ways to compute a “center” of the envelope, ranging from the  
 273 average of the two end points, to a centroid calculation, to computing the point where the integral  
 274 of CKE over distance is balanced on both sides, which we call the “half-power point.” We have  
 275 selected the latter to use, as it defines a “center” closer to the peak of CKE in the envelope. This  
 276 is advantageous when the CKE curve is slightly skewed, with less magnitude on one side and  
 277 more on the other. Assuming that the variability (and hence CKE) would be highest near the  
 278 front (i.e., what is assumed in studies using the gradient method), finding a center of the  
 279 envelope that is biased toward peak CKE is a reasonable approach.

280 The half-power point ( $x_{mid}$ ) is computed so that

$$281 \int_{x_{south}}^{x_{mid}} CKE(x) dx = \frac{1}{2} \int_{x_{south}}^{x_{north}} CKE(x) dx, \quad (4)$$

282 where  $x_{south}$  and  $x_{north}$  are computed by first finding the maximum of CKE in the envelope above  
 283  $200 \text{ cm}^2 \text{ s}^{-2}$ , then finding the first value to the north just below 25% of that peak along with the  
 284 similar value to the south (shown in Figure 3). Values other than 25% of the peak were tested.  
 285 Using value greater than this, up to 50%, resulted in no significant difference in the half-power  
 286 point. Using values smaller resulted in some boundaries not being defined. Thus, 25% of peak  
 287 CKE was considered reasonable. If multiple regions of enhanced CKE were found along the

288 same track, this process was carried out for each of them. This was done for all the 24-year mean  
289 CKE profiles to establish the mean locations of the fronts between 1993 and 2016.

290 A similar procedure was done for CKE averaged over discrete 3-year intervals, starting in  
291 January 1993 and ending in December 2016. A 3-year average was used to reduce the influence  
292 of individual eddies on determining the envelope, and to reduce interannual variations in the  
293 front position, which have been observed in other studies at some locations (e.g., Kim and Orsi,  
294 2014; Shao et al., 2015). In particular, Kim and Orsi (2014) and Shao et al. (2015) found  
295 significant correlation with the Southern Annular Mode, which has a quasi-biennial oscillation  
296 (Hibbert et al., 2010). By averaging over three years, we found 8 distinct, statistically  
297 uncorrelated samples of CKE for each groundtrack from which to deduce shifts in the half-power  
298 point. We tested different averaging periods (ranging from 1- to 4-years), but found the estimate  
299 in overall shift of the half-power point over the 24-year period was insensitive to the choice.

300

### 301 **3. RESULTS AND ANALYSIS**

302 The first thing tested was how well CKE represented the full EKE. If CKE does not have the  
303 same general shape as EKE, then using it as a proxy for EKE to determine high energy envelopes  
304 is not valid. After finding satellite passes with high CKE as discussed in Section 2, EKE was  
305 computed along the same pass, using the crossover method (Equations 1 and 2).

306 Although CKE is lower than EKE along all groundtracks (see Figure 5 for examples), the  
307 pattern of KE rise then fall is virtually identical. CKE, however, has the benefit of higher and  
308 more regular sampling. Thus, we conclude CKE is a reasonable proxy for locating front positions  
309 even though it may not be useful for quantifying the full energy of the anomalous currents.

310 Four general types of enhanced CKE were found (Figures 4 and 5). In most regions, the  
311 envelope in CKE is more or less symmetrical (52% of cases). Only a few profiles have two  
312 distinct regions of enhanced CKE that were identified, with a clearly defined minimum below  
313  $200 \text{ cm}^2 \text{ s}^{-2}$  between them in all time periods (3% of cases). 20% of the passes have multiple  
314 peaks that vary in time but have no consistent minimum between the peaks (i e., Figure 4), while  
315 25% have a skewed envelope (Figure 5), with a long rise in CKE followed by a sharp drop-off.  
316 In all cases, though, the shape of the CKE envelope closely follows that of EKE, although the  
317 amplitude was attenuated, by anywhere from 25-50%. Having closer samples of CKE, however,  
318 allows for a better computation of the half-power point and possible shifts.

319 Figure 6 shows the locations of the half-power points determined from the mean CKE  
320 profiles, along with estimate of the front position based on different methods: density gradients  
321 from historical hydrographic sections (Orsi et al., 1995), dynamic topography contours (Kim and  
322 Orsi, 2014), and the gradient of sea surface temperature (Freeman and Lovenduski, 2016a).  
323 There are two estimates of the SAF and SACCF, and three of the PF. One of the PF estimates  
324 (from Freeman and Lovenduski, 2016a) includes the standard deviation of the daily estimates.

325 It is important to note the large differences in estimates for the same front, which indicates  
326 how difficult it is to determine fronts in a highly variable current system like the ACC. For  
327 instance, in the Indian Ocean at  $50^\circ\text{E}$ , Freeman and Lovenduski (2016a) find the PF at the same  
328 location that Orsi et al. (1995) found the SAF, while Kim and Orsi (2014) find it significantly  
329 farther south. The SAF determination using the contour method (Kim and Orsi, 2014) is  
330 substantially farther north than the one determined from hydrographic data (Orsi et al., 1995) at  
331 most longitudes. These differences are likely due to differences in the time-span, differences in

332 methodologies, and uncertainty in the data utilized. All lead to a level of uncertainty in the  
333 determination of a specific front at any time.

334 The half-power points of enhanced CKE generally occur near or between the fronts estimated  
335 by different methods (i.e., the three different PF estimates), indicating they are at least within the  
336 uncertainty bounds of frontal detection by other methods. Some values are at locations either  
337 north or south of the other front estimates by as much as  $3^\circ$ , but it should be noted that the  
338 standard deviation of the PF estimated by Freeman and Lovenduski (2016a,b) averages  $2\text{-}3^\circ$ .  
339 Using a PF variability statistic as an indicator of variability of all fronts, one can conclude the  
340 location CKE half-power points are well within the level of expected frontal variability and so  
341 not statistically too distant from a front location.

342 One may question whether the relatively wide envelopes of enhanced CKE overlap more  
343 than one front. This is a possibility, but if both fronts have moved south as some have argued  
344 (e.g., Sokolov and Rintoul, 2009b), then the CKE envelope should also shift, regardless of  
345 whether it includes one or two fronts. If the exact frontal location was known at any time, one  
346 could judge how well the CKE envelope (or half-center) point was associated with just one front.  
347 But considering the disagreement in climatologies (e.g., Figure 5) and the intrinsic variability of  
348 the front, this is impossible to test. One can, however, compute the distance from the CKE half-  
349 power point to the southern boundary (for those points that are nearest a climatological SAF  
350 position) and the distance with the northern boundary (for those that are nearest the PF) and  
351 compare this to the distance between the climatological positions of these fronts. Note that the  
352 distances must be computed along the groundtracks and not simply taken as the meridional  
353 distance at the longitude of the CKE half-power point.

354 The average distance between the half-power point and either northern or southern boundary  
355 is 541 km with a standard deviation of 196 km. The average distance between the Kim and Orsi  
356 (2014) PF and SAF along the groundtrack passes is 706 km with a standard deviation of 407 km.  
357 We used the Kim and Orsi (2014) front positions as these data was on a regular grid which made  
358 interpolation to the groundtrack positions easier and it was computed over the roughly the same  
359 time span as the CKE estimates. From these statistics, we conclude the CKE envelopes should  
360 generally only encompass either the PF or the SAF, although even if they did not, it should not  
361 preclude one from using statistics of the CKE half-power point to deduce shifts in the fronts,  
362 provided they are both shifting, as has been theorized.

363 Another method for determining frontal position is to examine the probability of jets  
364 occurring (Chapman, 2017a) (Figure 7). The CKE-defined mean front positions lie within the  
365 probability envelopes, giving more confidence that the CKE measure is providing a comparable  
366 measure of frontal position in many areas. The only location where CKE-defined fronts don't  
367 agree well with the probability field from Chapman (2017a) is just west of the dateline, where  
368 two points lie between levels of high jet (and hence front) probability. However, it should be  
369 noted that Chapman finds jets in the two areas north and south of the CKE half-power points less  
370 than 10% of the time and that the northern cluster lies on the northern edge of the enhanced CKE  
371 envelope. Although the half-power points are slightly south of this along these two passes, this is  
372 due to high CKE (in excess of  $200 \text{ cm}^2 \text{ s}^{-2}$ ) down to  $58^\circ\text{S}$ , where Chapman (2017a) detects few  
373 jets. It is unclear why Chapman (2017a) detects few jets in this region of high CKE, but it should  
374 be noted that this represents only 1% of the samples compared.

375 The comparison between CKE half-power points and front climatologies is reassuring that the  
376 method developed in Section 2 is successfully detecting regions of high energy related to jets

377 around fronts. Since the movement of jet positions has been used to estimate movement of the  
378 fronts (e.g., Chapman, 2017a), a comparable calculation with positions of high CKE seems  
379 reasonable. The majority of the estimated half-power points follows the SAF and is most likely  
380 due to the front (and jets) moving perpendicular to the groundtracks. This method will tend to  
381 only detect high CKE when the front is moving from northwest-to-southeast for an ascending  
382 pass, and from southwest-to-northeast for a descending pass. This method also only works in  
383 regions where the front is associated with highly variable jets, which does not occur at every  
384 longitude along the front (e.g., Chapman, 2017a).

385 To quantify movement of the envelope of enhanced CKE, a linear trend is fit to the 8  
386 estimations of the half-power point from 1993-2016 for each location shown in Figures 5 and 6.  
387 Analysis of the residuals about the trend indicated they were random (lag-1 autocorrelation  $< 0.1$   
388 for all cases), so standard error was computed by scaling the formal error from the covariance  
389 matrix determined in ordinary least squares by the standard deviation of the residuals. This was  
390 also scaled up to account for the degrees of freedom lost by estimating the trend by  $\sqrt{n/n_{EDOF}}$ ,  
391 where  $n = 8$ , and  $n_{EDOF} = 6$ . Finally, the 90% confidence interval was computed by scaling by  
392 1.94 for 6 effective degrees of freedom assuming a normal t-distribution of the residuals.

393 The results indicate considerable regional variability in the change of the half-power point  
394 over 24 years, with large uncertainty bars (Figure 8). This is due to the substantial temporal  
395 variability in the positions, which can be seen in Figure 4, where the leading edge of the CKE  
396 envelope varies by over 1 degree of latitude (over 100 km) between 1993-1995 and 2011-2012.  
397 To better see significant changes outside the uncertainty (90% confidence) interval, one can  
398 compute the signal to noise ratio (SNR = trend/uncertainty). Examining this (Figure 9), one can  
399 see there are some regions where the half-power point has moved southward by a significant

400 distance over the last 24 years (13.6% of points), but there are also points where it has moved  
401 north (9.6%). For the majority of points (76.8%), there is no statistically significant change,  
402 meaning no movement of the front is as likely as either a southward or northward shift due to the  
403 high variability in 3-year positions.

404

#### 405 **4. DISCUSSION AND CONCLUSIONS**

406 The results from the analysis of the positions of enhanced kinetic energy suggest no overall  
407 shift in the frontal positions across the Southern Ocean, but some large, localized movements.  
408 The region indicative of some southward shift between 90°E and 170°E is in approximately the  
409 same area where Kim and Orsi (2014) and Freeman and Lovenduski (2016a) also reported large  
410 shifts, between 1992 to 2011 and 2002 and 2014, respectively. However Freeman and  
411 Lovenduski only examined the Polar front, and Kim and Orsi (2014) only found large shifts in  
412 the PF and the southern ACC front. They found shifts of order 50-100 km in the SAF where the  
413 points in this study cluster, which is considerably smaller than the individual shifts we find  
414 between 90°E and 170°E along the SAF. However, the overall average over the region between  
415 90°E and 170°E (-29 km per decade, or -66.7 km in 23 years), is consistent with what Kim and  
416 Orsi (2014) found.

417 Kim and Orsi (2014) and Freeman and Lovenduski (2016a) also found slight northward  
418 shifts in the front positions in the southeast Pacific, between 200°E-270°E. We find some  
419 locations in this region, where the CKE half-power points cluster around the SAF, also have a  
420 significant northward shift. Kim and Orsi (2014) found the shift of the SAF was about 30-40 km  
421 between 1992 and 2011. Our results suggest larger shifts in some areas; averaged over the area,

422 our results are 46 km per decade to the north, or 106 km from 1993-2015, which is consistent  
423 with the average over the region computed by Freeman and Lovenduski (2016a) from sea surface  
424 temperature data, but for the Polar Front.

425 Kim and Orsi (2014) suggest that the shift of the fronts in the Indian Ocean were not directly  
426 related to shifts in winds, but instead were caused by an expansion of the Indian subtropical gyre.  
427 They linked the shift in the southeastern Pacific to wind changes related to mainly the Southern  
428 Annular Mode in that region (Kim and Orsi, 2014).

429 Overall, this study supports the recent studies by Kim and Orsi (2014), Gille (2014), Freeman  
430 and Lovenduski (2016a), and Chapman (2017a). All find that, while the frontal positions of the  
431 ACC are highly variable in time, there is no statistically significant shift in the fronts to the south  
432 on average. This study utilized a novel technique to reach this conclusion, which adds to the  
433 robustness of evidence that there has not been a shift in the frontal positions. Thus, while the  
434 fronts may eventually shift south in a warming climate, there is no strong evidence that it is  
435 happening at the moment.

436 Other studies have shown significant positive trends in the Southern Ocean that have been  
437 connected to the warming climate. These include changes in the ocean heat content in the upper  
438 ocean between the 1930s-1950s and 1990s (e.g., Böning et al., 2008; Gille, 2008), increases in  
439 the heat content of deep water between the 1990s and 2005 (e.g., Purkey and Johnson, 2010),  
440 and increases in eddy kinetic energy in the Indian and Pacific Oceans since 1993 (Hogg et al.,  
441 2015). Observational evidence of shifts in the winds, however, indicates that while there may be  
442 a slight southward shift in winds during the southern hemisphere summer, the overall yearly  
443 average shift is not significant (Swart and Fyfe, 2012). Thus, the growing consensus that fronts



444 have not shifted to the south, on average, is consistent with observations of no significant shift in  
445 the yearly averaged winds.

446 The only evidence supporting a hypothesis that ACC fronts have shifted southward since the  
447 1990s comes from mapping the location of contours of constant dynamic topography over time  
448 (e.g., Sokolov and Rintoul, 2009b; Kim and Orsi, 2014). As Gille (2014) argued and as we have  
449 demonstrated based on a simple thought experiment (Figure 1), there are other equally plausible  
450 explanations for the apparent southern shift of the contours. Considering that four different  
451 techniques – location of mean transport (Gille, 2014), maximum SST gradients (Freeman and  
452 Lovenduski, 2016a), probability of jet positions (Chapman, 2017a), and the location of enhanced  
453 kinetic energy (this study) – all agree that the fronts have not moved significantly on average,  
454 one has to conclude that the method of using dynamic topography contours to detect changes in  
455 front position is too sensitive to sea level rise to be useful for determining shifts in frontal positions,  
456 although it may prove useful for determining the mean position as Chapman (2017a) has argued.

457

458

459 **Acknowledgements**

460 The author would like to thank Christopher Chapman and an anonymous reviewer for their  
461 extensive comments on an earlier draft of this paper. Their many suggestions helped the author  
462 improve the paper substantially. This research was carried out under grant number  
463 NNX13AG98G from NASA and a grant from NOAA for the NASA/NOAA Ocean Surface  
464 Topography Science Team.

465 **REFERENCES**

- 466 Andersen O B, and Knudsen P: DNSC08 mean sea surface and mean dynamic topography  
467 models, *J. Geophys. Res.*, 114, C11001, doi:10.1029/2008JC005179, 2009.
- 468 Beckley, B.D., Zelensky, N.P., Holmes, S.A., Lemoine, F.G., Ray, R.D., Mitchum, G.T., Desai,  
469 S., and Brown, S. T.: Assessment of the Jason-2 Extension to the TOPEX/Poseidon, Jason-1  
470 Sea-Surface Height Time Series for Global Mean Sea Level Monitoring, *Marine Geodesy*,  
471 33(S1): 447-471, Supplemental Issue on OSTM/Jason-2 calibration/validation, Vol. 1, DOI:  
472 10.1080/01490419.2010.491029, 2010
- 473 Belkin, I. M., and Gordon, A. L.: Southern Ocean fronts from the Greenwich meridian to  
474 Tasmania, *J. Geophys. Res.*, 101, 3675–3696, 1996.
- 475 Böning C. W., Dispert A., Visbeck M., Rintoul S. R., Schwarzkopf F. U.: The response of the  
476 Antarctic circumpolar current to recent climate change. *Nat Geosci.*, 1, 864–869, 2008.
- 477 Chapman, C. C.: Southern Ocean jets and how to find them: Improving and comparing common  
478 jet detection methods, *J. Geophys. Res. Oceans*, 119, 4318–4339,  
479 doi:10.1002/2014JC009810, 2014.
- 480 Chapman, C. C., New perspectives on frontal variability in the Southern Ocean, *J. Phys. Ocean.*,  
481 47, 1151-1168, doi:/10.1175/JPO-D-16-0222.1, 2017a.
- 482 Chapman, C. C., Data from: New perspectives on frontal variability in the southern ocean. Dryad  
483 Digital Repository. <http://dx.doi.org/10.5061/dryad.q9k8r>, 2017b.
- 484 Chelton, D. B., M. G. Schlax, R. M. Samelson, and R. A. de Szoeke: Global observations of  
485 large oceanic eddies, *Geophys. Res. Lett.*, 34, L15606, doi:10.1029/2007GL030812, 2007.
- 486 Cunningham, S. A., Alderson, S. G. , King, B. A., and Brandon, M. A.: Transport and variability  
487 of the Antarctic Circumpolar Current in Drake Passage, *J. Geophys. Res.*, 108(C5), 8084,  
488 doi:10.1029/2001JC001147, 2003
- 489 Dong, S., Sprintall, J., and Gille, S. T. : Location of the Antarctic Polar Front from AMSR-E  
490 Satellite Sea Surface Temperature measurements, *J. Phys. Oceanogr.*, 36, 2075–2089,  
491 doi:10.1175/JPO2973.1, 2006.
- 492 Ducet, N., Le Traon, P.-Y., Reverdin, G.: Global high resolution mapping of ocean circulation  
493 from TOPEX/Poseidon and ERS-1 and -2. *Journal of Geophysical Research* 105 (C8),

494 19477–19498, 2000.

495 Fyfe, J. C., and Saenko, O. A.: Simulated changes in the extratropical Southern Hemisphere  
496 winds and currents, *Geophys. Res. Lett.*, 33, L06701, doi:10.1029/2005GL025332, 2006.

497 Freeman, N. M., Lovenduski, N. S.: Mapping the Antarctic polar front: weekly realizations from  
498 2002 to 2014, *Earth System Science Data*, 8, 191-198, doi:10.5194/essd-8-191-2016, 2016a.

499 Freeman, N. M., Lovenduski, N. S.: Mapping the Antarctic polar front: weekly realizations from  
500 2002 to 2014, links to NetCDF file and MPEG4 movie, PANGEA,  
501 doi:10.5194/PANGEA.855640, 2016b.

502 Gille, S: Decadal-scale temperature trends in the Southern Hemisphere Ocean, *J Climate*, 21,  
503 4749–4765, 2008

504 Gille, S. T.: Meridional displacement of the Antarctic Circumpolar Current, *Philos. Trans. R.*  
505 *Soc. A*, 372, 20130273, doi:10.1098/rsta.2013.0273, 2014.

506 Graham, R. M., De Boer, A. M., Heywood, K. J., Chapman, M. R., and Stevens, D. P.: Southern  
507 Ocean fronts: Controlled by wind or topography?, *J. Geophys. Res. Oceans*, 117, C08018,  
508 doi:10.1029/2012JC007887, 2012.

509 Hibbert A, Leach H, Woodworth P, Hughes C, Roussenov V.: Quasi-biennial modulation of the  
510 Southern Ocean coherent mode, *Q. J. R. Meteorol. Soc.*, 136, 755 – 768.  
511 DOI:10.1002/qj.581, 2010.

512 Hogg, A. McC., Meredith, M. P., Chambers, D. P., Abrahamsen, E. P., Hughes, C. W., and  
513 Morrison, A. K.: Recent trends in the Southern Ocean eddy field, *J. Geophys. Res. Oceans*,  
514 120, 257–267, doi:10.1002/2014JC010470, 2015.

515 Kim, Y. S., and Orsi, A. H.: On the variability of Antarctic Circumpolar Current fronts inferred  
516 from 1992–2011 altimetry, *J. Phys. Oceanogr.*, 44, 3054–3071, doi:10.1175/JPO-D-13-  
517 0217.1, 2014.

518 Langlais, C., Rintoul, S. R., and Schiller, A.: Variability and mesoscale activity of the Southern  
519 Ocean fronts: Identification of a circumpolar coordinate system, *Ocean Modell.*, 39, 79–96,  
520 doi:10.1016/j.ocemod.2011.04.010, 2011.

521 Moore, J. K., Abbott, M. R., and Richman, J. G.: Location and dynamics of the Antarctic Polar  
522 Front from satellite sea surface temperature data, *J. Geophys. Res.*, 104, 3059–3073,  
523 doi:10.1029/1998JC900032, 1999.

524 Nowlin, W. D., and Clifford, M.: The kinematic and thermohaline zonation of the Antarctic  
525 Circumpolar current at Drake Passage, *J. Mar. res.*, 40, 481-507, 1995.

526 Orsi, A. H., Whitworth III, T., and Nowlin Jr., W. D.: On the meridional extent and fronts of the  
527 Antarctic Circumpolar Current, *Deep Sea Res., Part I*, 42(5), 641–673, doi:10.1016/0967-  
528 0637(95)00021-W, 1995.

529 Parke, M. E., Stewart, R. H., Farless, D. L., and Cartwright, D. E.: On the choice of orbits for an  
530 altimetric satellite to study ocean circulation and tides, *J. Geophys. Res.*, 92, 11693–11707,  
531 1987.

532 Pujol, M.-I., Faugere, Y., Taburet, G., Dupuy, S., Pelloquin, C., Ablain, M., Picot, N., DUACS  
533 DT2014: the new multi-mission altimeter data set reprocessed over 20 years, *Ocean. Sci.*, 12,  
534 1067-1090, doi:10.5194/os-12-1067-2016, 2016.

535 Purkey, S. G., and Johnson, G. C.: Warming of global Abyssal and deep southern ocean waters  
536 between the 1990s and 2000s: Contributions to global heat and sea level rise budgets, *J.*  
537 *Clim.*, 23, 6336–6351, doi:10.1175/2010JCLI3682.1, 2010.

538 Sallee, J. B., Speer, K., and Morrow, R.: Response of the Antarctic Circumpolar Current to  
539 atmospheric variability, *J. Clim.*, 21(12), 3020–3039, doi:10.1175/2007JCLI1702.1, 2008.

540 Shao, A. E., S. T. Gille, S. Mecking, and L. Thompson: Properties of the Subantarctic Front and  
541 Polar Front from the skewness of sea level anomaly, *J. Geophys. Res. Oceans*, 120,  
542 5179–5193, doi:10.1002/2015JC010723, 2015.

543 Sokolov, S., and Rintoul, S. R.: Multiple jets of the Antarctic Circumpolar Current south of  
544 Australia, *J. Phys. Oceanogr.*, 37, 1394–1412, doi:10.1175/JPO3111.1, 2007.

545 Sokolov, S., and Rintoul, S. R.: Circumpolar structure and distribution of the Antarctic  
546 Circumpolar Current fronts: 1. Mean circumpolar paths, *J. Geophys. Res.*, 114, C11018,  
547 doi:10.1029/2008JC005108, 2009a.

548 Sokolov, S., and Rintoul, S. R.: Circumpolar structure and distribution of the Antarctic  
549 Circumpolar Current fronts: 2. Variability and relationship to sea surface height, *J. Geophys.*  
550 *Res.*, 114, C11019, doi:10.1029/2008JC005248, 2009b.

551 Swart, N., and Fyfe, J. C.: Observed and simulated changes in the Southern Hemisphere surface  
552 westerly wind-stress. *Geophys. Res. Lett.*, 39, L16711, doi:10.1029/2012GL052810, 2012.

553 Thompson, A. F., Haynes, P. H., Wilson, C., and Richards, K. J.: Rapid Southern Ocean front  
554 transitions in an eddy-resolving ocean GCM, *Geophys. Res. Lett.*, 37, L23602,  
555 doi:10.1029/2010GL045386, 2010.

556 Thompson, A. F., and Richards, K. J.: Low frequency variability of Southern Ocean jets, *J.*  
557 *Geophys. Res.*, 116, C09022, doi:10.1029/2010JC006749, 2011.

558 Wunsch, C.: *The Ocean Circulation Inverse Problem*, 458 pp., Cambridge Univ. Press, Cambridge, Mass.

559  
560  
561

562 **Figure Captions**

563

564 **Figure 1.** a) Mean dynamic topography in the Southern Ocean along a north-south meridian for three  
565 scenarios, and b) the corresponding geostrophic velocity, with positive values indicating eastward flow.  
566 The scenarios are: an initial state (dashed black line), a shift of the two fronts south by 60 km with no  
567 change in magnitude or shape of the currents (red line), and no shift of the mean of the current, but a  
568 change in the magnitude and shape (blue line).

569

570 **Figure 2.** Positions of the T/P, Jason-1, Jason-2 and Jason-3 groundtracks used for this study (black  
571 lines), and the approximate locations of the Subantarctic Front (red line) and the Polar Front (blue  
572 line) as estimated by Orsi et al. (1995). The orange track shows the location of the pass used in analysis  
573 shown in Figures 3 and 4.

574

575 **Figure 3.** An example profile of mean CKE (1993-2016) along a ground track in the southern Indian  
576 Ocean (shown in orange in Figure 2), demonstrating the location of the half-power point and the locations  
577 of the southern and northern boundaries of the enhanced CKE envelope. See text for details of the  
578 computations.

579

580 **Figure 4.** Three-year averages of CKE estimated along pass shown in Figure 2 (solid lines) along with  
581 the long-term mean from 1993-2016 (dotted line).

582

583 **Figure 5.** Examples of the three types of CKE profiles found (black lines), along with the value of the full  
584 EKE computed at crossover points.

585

586 **Figure 6.** Mean positions of fronts estimated from CKE (orange dots) along with estimates from other  
587 authors: Orsi et al. (1995) computed using hydrographic sections, Kim and Orsi (2014) based on contours  
588 of dynamic topography, and Freeman and Lovenduski (2016a) based on gradients of sea surface  
589 temperature. The Orsi et al. (1995) fronts were downloaded from  
590 [https://gcmd.nasa.gov/records/AADC\\_southern\\_ocean\\_fronts.html](https://gcmd.nasa.gov/records/AADC_southern_ocean_fronts.html). The Freeman and Lovenduski fronts  
591 were downloaded from <https://doi.pangaea.de/10.1594/PANGAEA.855640> (Freeman and Lovenduski,  
592 2016b). The Kim and Orsi (2014) fronts were provided by Yong Sun Kim upon request.

593

594 **Figure 7.** Mean positions of fronts estimated from CKE (black dots) along with the percent occurrence of  
595 a jet between 1993 and 2014 computed by Chapman (2017a). Data were downloaded from  
596 <http://dx.doi.org/10.5061/dryad.q9k8r> (Chapman, 2017b). The percent occurrence of the jet was  
597 computed by calculating the number of times a jet occurred in the daily files, dividing by the total number  
598 of days between January 1993 and December 2014, and multiplying by 100.

599

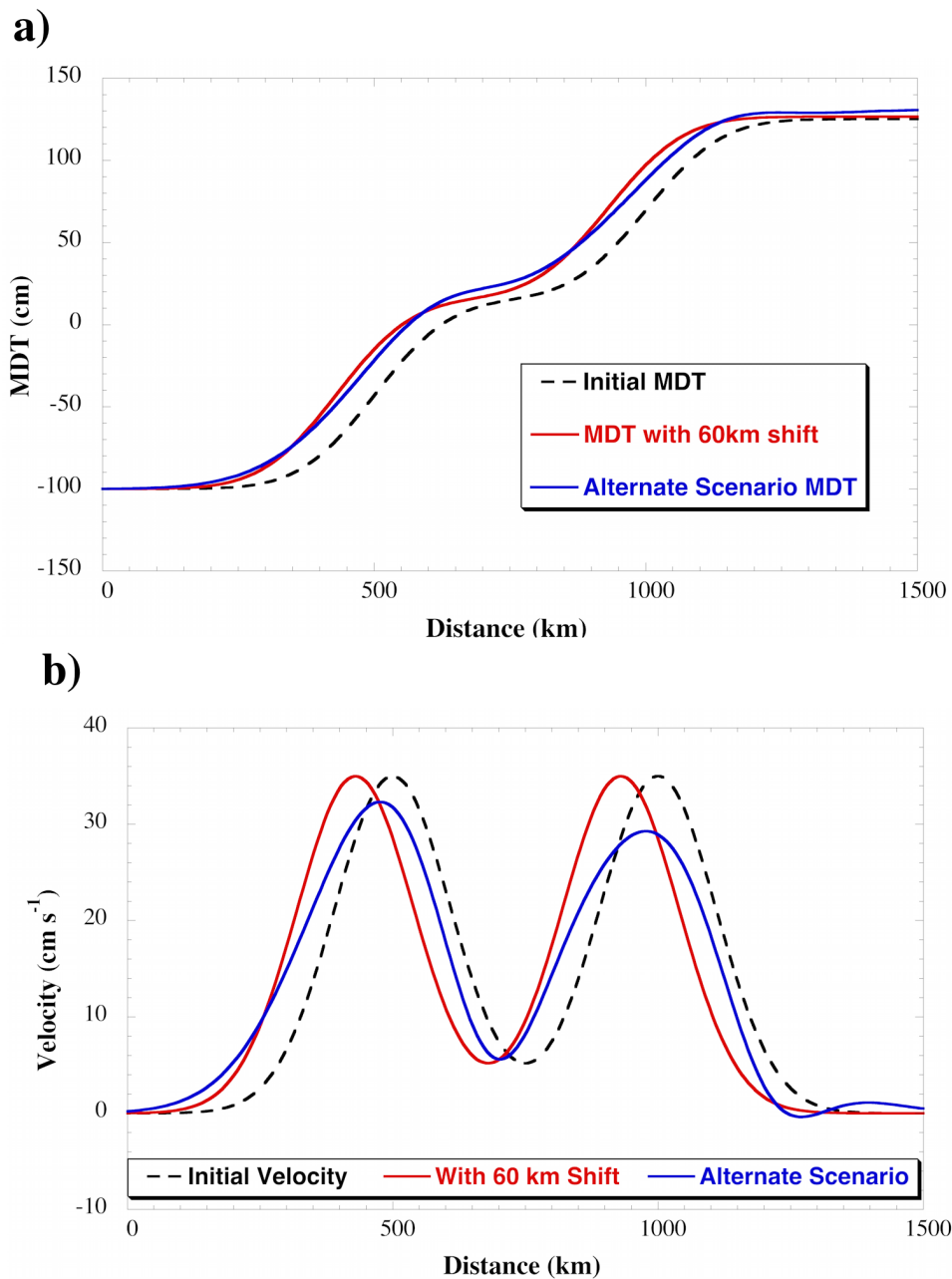
600 **Figure 8.** Estimated trend in the half-power point of CKE for each location shown in Figures 6 and 7, as a  
601 function of latitude. Error bars represent the 90% confidence interval.

602

603 **Figure 9.** SNR (trend/error in Figure 8). Values larger than 1 indicate a statistically significant northern  
604 shift. Values smaller than -1 indicate a statistically significant southern shift. Values between  $\pm 1$  indicate  
605 no statistically significant shift.

606

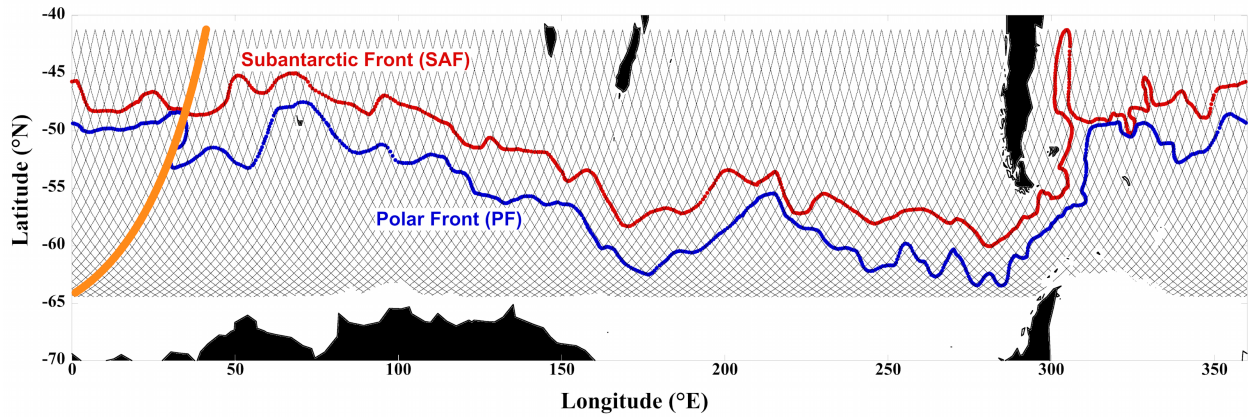
607



608  
 609  
 610  
 611  
 612  
 613  
 614  
 615  
 616

**Figure 1.** a) Mean dynamic topography in the Southern Ocean along a north-south meridian for three scenarios, and b) the corresponding geostrophic velocity, with positive values indicating eastward flow. The scenarios are: an initial state (dashed black line), a shift of the two fronts south by 60 km with no change in magnitude or shape of the currents (red line), and no shift of the mean of the current, but a change in the magnitude and shape (blue line).

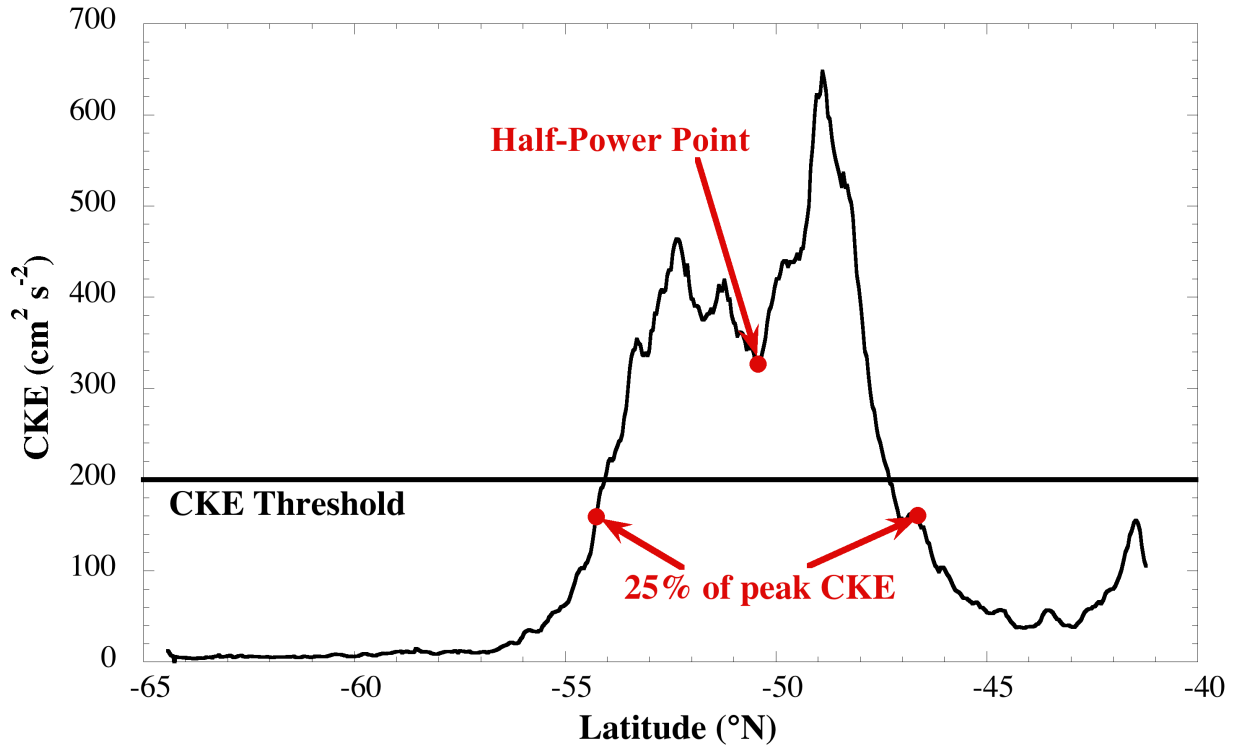
617  
618



619  
620  
621  
622  
623  
624  
625  
626

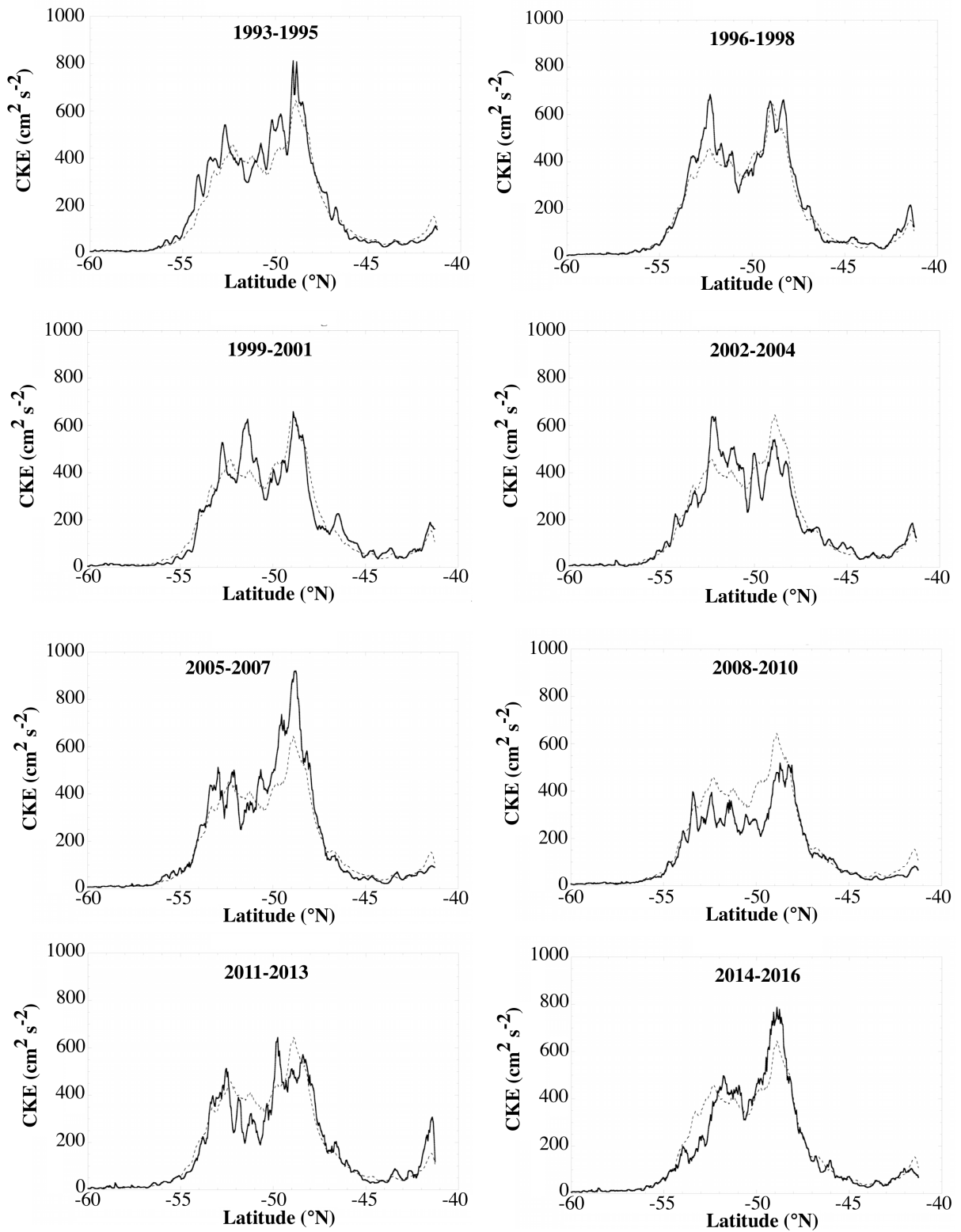
**Figure 2.** Positions of the T/P, Jason-1, Jason-2 and Jason-3 groundtracks used for this study (black lines), and the the approximate locations of the Subantarctic Front (red line) and the Polar Front (blue line) as estimated by Orsi et al. (1995). The orange track shows the location of the pass used in analysis shown in Figures 3 and 4.





627  
 628  
 629  
 630  
 631  
 632  
 633  
 634

**Figure 3.** An example profile of mean CKE (1993-2016) along a ground track in the southern Indian Ocean (shown in orange in Figure 2), demonstrating the location of the half-power point and the locations of the southern and northern boundaries of the enhanced CKE envelope. See text for details of the computations.

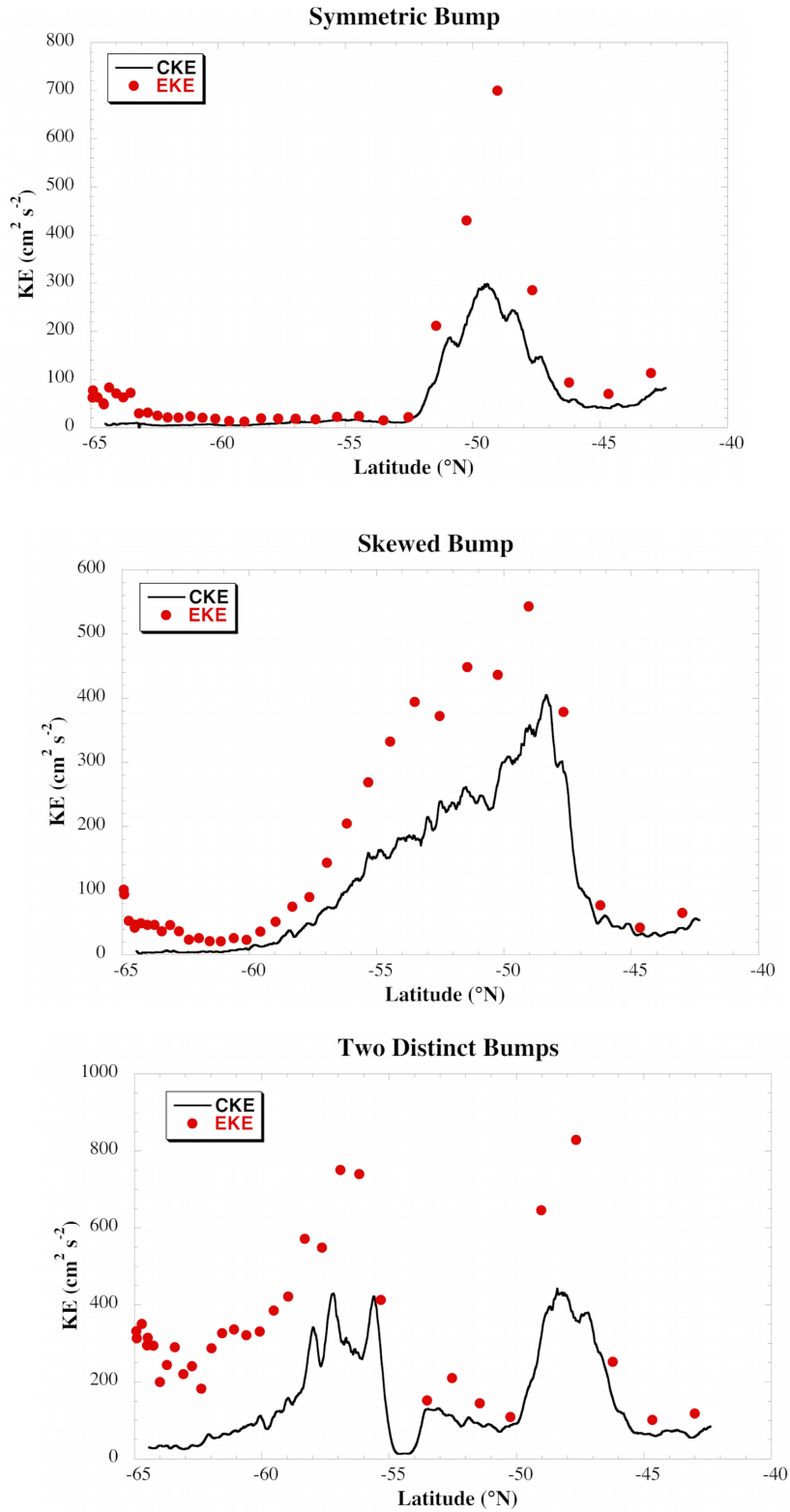


636

637

638

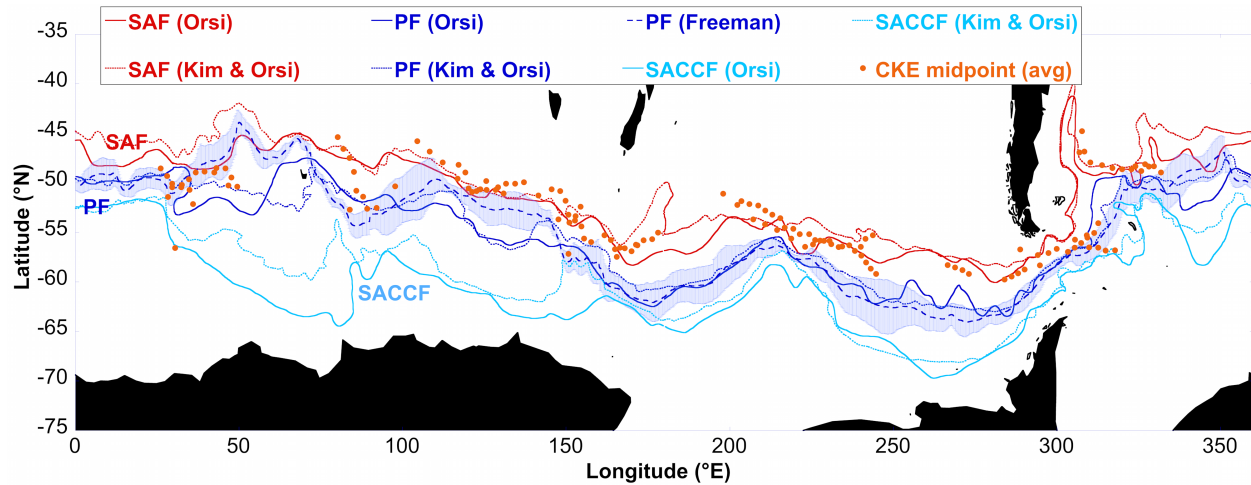
**Figure 4.** Three-year averages of CKE estimated along pass shown in Figure 2 (solid lines) along with the long-term mean from 1993-2016 (dotted line).



639  
640  
641  
642

**Figure 5.** Examples of the three types of CKE profiles found (black lines), along with the value of the full EKE computed at crossover points.

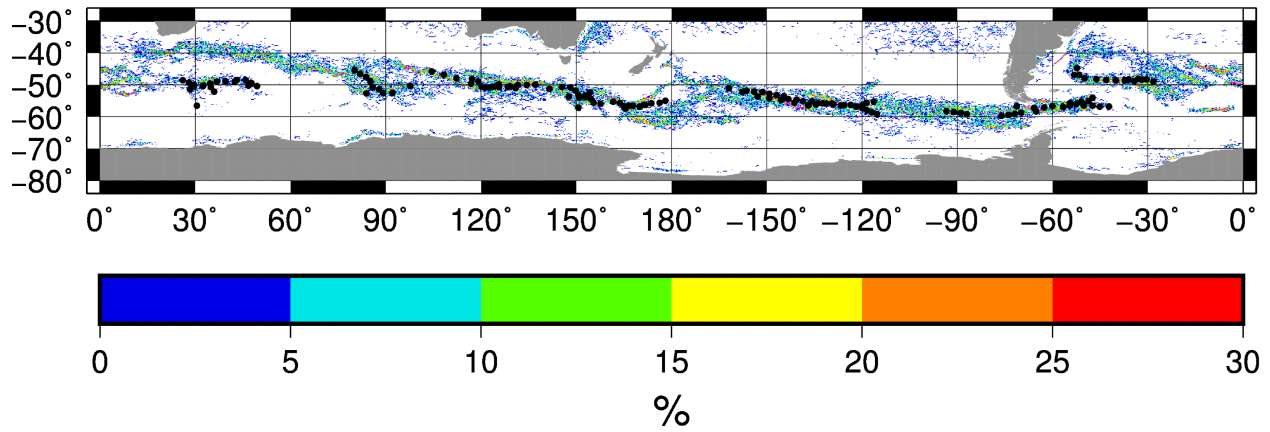
643  
644



645  
646  
647  
648  
649  
650  
651  
652  
653  
654  
655

**Figure 6.** Mean positions of fronts estimated from CKE (orange dots) along with estimates from other authors: Orsi et al. (1995) computed using hydrographic sections, Kim and Orsi (2014) based on contours of dynamic topography, and Freeman and Lovenduski (2016a) based on gradients of sea surface temperature. The Orsi et al. (1995) fronts were downloaded from [https://gcmd.nasa.gov/records/AADC\\_southern\\_ocean\\_fronts.html](https://gcmd.nasa.gov/records/AADC_southern_ocean_fronts.html). The Freeman and Lovenduski fronts were downloaded from <https://doi.pangaea.de/10.1594/PANGAEA.855640> (Freeman and Lovenduski, 2016b). The Kim and Orsi (2014) fronts were provided by Yong Sun Kim upon request.

656



657

658

659

660

661

662

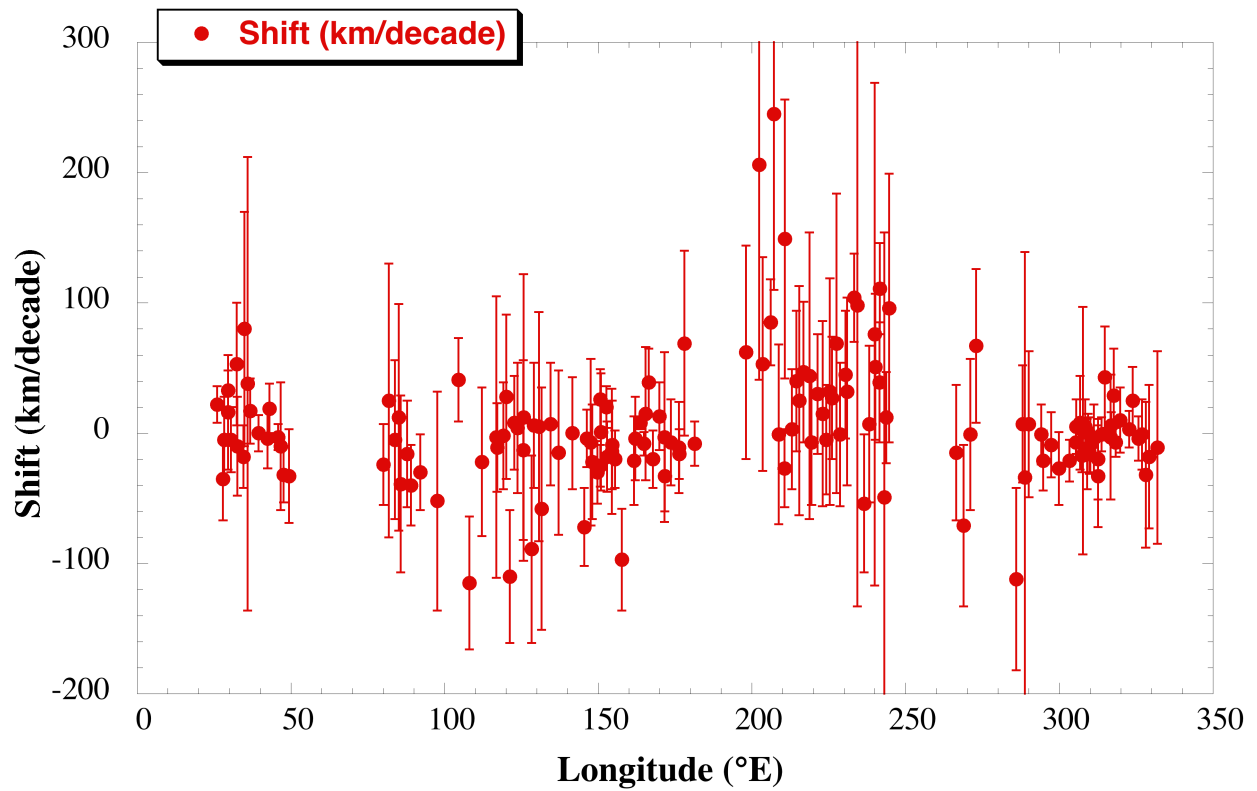
663

664

665

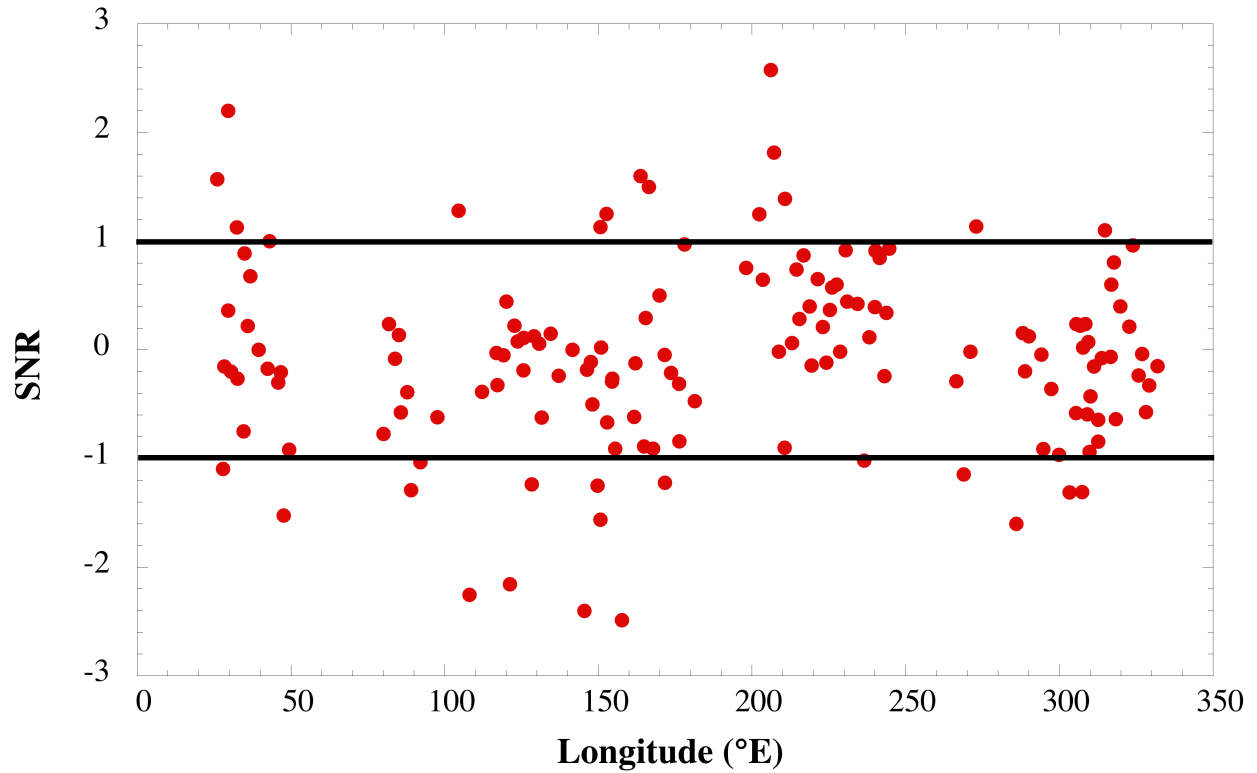
**Figure 7.** Mean positions of fronts estimated from CKE (black dots) along with the percent occurrence of a jet between 1993 and 2014 computed by Chapman (2017a). Data were downloaded from <http://dx.doi.org/10.5061/dryad.q9k8r> (Chapman, 2017b). The percent occurrence of the jet was computed by calculating the number of times a jet occurred in the daily files, dividing by the total number of days between January 1993 and December 2014, and multiplying by 100.

666



667  
668  
669  
670  
671

**Figure 8.** Estimated trend in the half-power point of CKE for each location shown in Figures 6 and 7, as a function of latitude. Error bars represent the 90% confidence interval.



672  
 673  
 674  
 675  
 676  
 677  
 678

**Figure 9.** SNR (trend/error in Figure 8). Values larger than 1 indicate a statistically significant northern shift. Values smaller than -1 indicate a statistically significant southern shift. Values between  $\pm 1$  indicate no statistically significant shift.